

Lead-free perovskite solar cells numerically modeled with inorganic charge transfer materials

Dinesh Kumar Thakre¹, V. K. Suman²

1. Dinesh Kumar Thakre, PhD Scholer, Department of Physics, Malwanchal University, Indore, MP, India,

2. V. K. Suman, Professor, Department of Physics, Malwanchal University, Indore, MP, India

Abstract

Background: Photovoltaic research continues to focus on organic-inorganic hybrid perovskites, ten years after they were originally mentioned in a report on the deployment of solar cells. Appropriate material selection for various layers has allowed for high power conversion efficiency (PCE) values, which currently exceed 24 percent. Unfortunately, poisonous lead is included in metal halide perovskite solar cells (PSCs), which poses a significant risk to their commercialization. scientific into lead-free metal halide perovskite is being conducted extensively by the PSC scientific community in an effort to address lead toxicity concerns in perovskite-based solar cells. A unique configuration for solar cells is proposed in this study, consisting of FTO, Transition Metal Di-Chalcogenides, Perovskite, Copper Thiocyanate, and Au. Since tungsten disulfide has a high electron mobility, it is utilized as an electron transport metal (ETM) in these transition metal di-chalcogenides. Copper thiocyanate (CuSCN), on the other hand, is used as a hole transport metal (HTM) because of its excellent band alignment with perovskite and high transparency. The effect of perovskite layer, electron transport layer, and hole transport layer thickness variations on performance metrics was investigated. At the ideal perovskite layer thickness of 700 nm, a PCE of 19.84% is attained. Due to an increase in electron-hole pair recombination, PCE decreases as thickness exceeds 700 nm. . Impact of interfacial defects on the performance parameter was also scrutinized. Simulation results reveal that the interfacial defect of ETM/Perovskite has a larger impact on performance parameters than that of Perovskite/HTM defect when light is irradiated from the ETM side. We also investigated the effect of temperature variation on device performance. The PSC showed optimum performance in the range of 20 °C to 50 °C and the ideal working temperature was viewed as 30 °C.

I. INTRODUCTION

A perovskite solar cell is the new buzz in the scientific community, where it is commonly referred as photovoltaic technology based on organo-metallic hybrid perovskite. The Photovoltaic community prefers this due to their high efficiency, low fabrication costs and ease of fabrication [1]. The inception of Perovskite Solar Cell (PSC) can be traced back to 2009, when the incorporation of perovskite material into dye-sensitized solar cell marked its beginning [2]. It is considered as one of the promising technologies for future power generation from solar radiation. The power conversion efficiency of perovskite solar cells have been improved from 3.8% in 2009 to recently certified 24.2% [3-9].

The performance of solar cells over a 40-year period has been studied using numerical simulations [10]. In 1975, Jerry offered a useful analytical method for discussing the carrier transport issue with silicon solar cells by resolving Poisson's equation and continuity equations for holes and electrons [11]. In order to comprehend the workings of solar cells, a number of software applications, including AMPS-1D, PC1D, and SCAPS-1D, are frequently utilized for thin film solar cells [12]. Numerous researchers have also investigated and developed the numerical analysis for dye-sensitized solar cells (DSCs) [13–15]. An improved knowledge of the mechanics in solar cells has been obtained with the development of these numerical models, which in turn helps to advance the device towards improved efficiency.

For perovskite solar cells, a numerical model based on Poisson's equation and continuity equations has been created. To minimize computation complexity, this model has been simplified as much as possible under certain suitable assumptions. Furthermore, this chapter introduces the specifics of computation methodologies and procedures. The simulation results, which are produced using Matlab, are utilized to comprehend the effects of band gap energy, relative dielectric permittivity, and effective density of state on perovskite solar cell performance.

Proposed perovskite based solar cell

The proposed Proposed Perovskite based Solar Cell composed of different layered structure as depicted. When light is irradiated on the lead-free perovskite layer, photogenerated carriers (electron-hole pairs). Are generated for those photons whose energy is greater than the bandgap of perovskite absorber. These photogen-erated carriers are collected by electron and hole charge transport layer. The collection of photogenerated carriers fully depends on band position ETM and

Computational modeling of proposed device

Regular PSC accompanying a configuration of FTO/WS2/Perovskite/CuSCN/Au is computationally Modeled using SCAP software. SCAP is developed by Prof. Burgelman and his team at Gent University, Belgium. It is initially designed for CdTe based multilayer Solar cell. Here an attempt is being made to numerically model perovskite solar cell using same software. SCAP solves three basic differential equations such as diffusion equations for both electron and hole and continuity equation in position

Physics Model in PSCs Basic Equations

In this section, a one-dimensional model is established by using Poisson's equation and continuity equations to describe the performance of perovskite solar cells. The effects of defect density and ionised doping density are not considered in this model, so the Poisson's equation can be given by:

$$\frac{\partial^2 \varphi(x)}{\partial x^2} = \frac{q}{\epsilon} [n(x) - p(x)] \quad (2.01)$$

where φ is the potential, q is the elementary charge, ϵ is the permittivity, n and p are the density of free electrons and the density of free holes respectively.

The continuity equations of electrons and holes can be described by:

$$q \frac{\partial n}{\partial t} = \frac{\partial J_n}{\partial x} + qG - qR \quad (2.02)$$

$$q \frac{\partial p}{\partial t} = -\frac{\partial J_p}{\partial x} + qG - qR \quad (2.03)$$

where J_n is the electron current density, J_p is the hole current density, G is the optical generation rate, R is the recombination rate.

Under a steady state condition, electron and hole densities do not change with time, so the continuity equations can be simplified as:

$$\frac{\partial J_n}{\partial x} = -qG + qR \quad (2.04)$$

$$\frac{\partial J_p}{\partial x} = qG - qR \quad (2.05)$$

In a perovskite solar cell, the output current includes diffusion current and drift current caused by electrons and holes. It can be obtained from the following equations:

$$J_n = J_{diffusion} + J_{drift} = qn\mu_n \frac{\partial \varphi}{\partial x} + qD_n \frac{\partial n}{\partial x} \quad (2.06)$$

$$J_p = J_{diffusion} + J_{drift} = -qp\mu_p \frac{\partial \varphi}{\partial x} + qD_p \frac{\partial p}{\partial x} \quad (2.07)$$

where D_n is the electron diffusion coefficient, D_p is the hole diffusion coefficient, μ_n is the electron mobility, and μ_p is the hole mobility. In this model, it is assumed that $D_{n,p}$ and $\mu_{n,p}$ meet the Einstein relation, which can be expressed as

$$D_{n,p} = \mu_{n,p} \frac{k_B T}{q} = V_t \quad (2.08)$$

where k_B is the Boltzmann constant, and T is the temperature.

There are three unknowns to be solved, which are n , p and φ . In order to obtain these values, appropriate boundary conditions are required. At the cathode and anode, density of electrons and holes obey the Boltzmann distribution, and they can be expressed as:

$$n(0) = N_c e^{\frac{E_c - E_{fn}}{-k_B T}} \quad (2.09)$$

$$p(L) = N_c e^{\frac{E_v - E_{fp}}{k_B T}} \quad (2.10)$$

in which, N_c is the density of state, E_{fn} and E_{fp} are the electron and hole Quasi-Fermi level. In perovskite solar cells, the output voltage is equal to the difference between E_{fn} and E_{fp} without considering the work function of the metal electrode, and it can be expressed as:

$$\varphi = E_{fn} - E_{fp} = E_{gap} + k_B T \ln\left(\frac{n(0)}{N_c}\right) + k_B T \ln\left(\frac{p(L)}{N_c}\right) \quad (2.11)$$

Here, in order to simplify the device model, it assumes that the output voltage value is the bandgap energy of the perovskite, and the corresponding boundary conditions can be given by

$$\varphi_{(L)} - \varphi_{(0)} = V_a - E_{gap} \quad (2.12)$$

$$\begin{cases} n_{(0)} = N_c \\ n_{(L)} = N_c \exp\left(-\frac{E_{gap}}{V_t}\right) \end{cases} \quad (2.13)$$

$$\begin{cases} p_{(L)} = N_c \\ p_{(0)} = N_c \exp\left(-\frac{E_{gap}}{V_t}\right) \end{cases} \quad (2.14)$$

where, V_a is the applied voltage.

Generation and Recombination Mechanism

In 2004, Hoppe showed that if the thickness of a device is very thin (under 100nm), the exponential relationship of light absorption and distance do not affect the performance of device significantly, so the generation rate can be set as a constant [16]. Here, the generation constant used for perovskite is difficult to find but the absorption coefficient can be easily found. Therefore, we still use the exponential model, and the charge generation rate can be given by:

$$G_{(x)} = \int_0^{\lambda_0} G(\lambda, x) d\lambda = \int_0^{\lambda_0} IPCE(\lambda) \frac{I(\lambda) \times \alpha(\lambda) \times e^{-\alpha(\lambda)x}}{hc/\lambda} d\lambda \quad (2.15)$$

where, IPCE is incident photon to current efficiency, $I_{(\lambda)}$ is the incident light density, $\alpha_{(\lambda)}$ is the absorption coefficient, h is the Plank constant, c is the light speed, λ is the photon's wavelength. Here, it assumes that IPCE is equal to 100%, which means all of the excitons can be separated to pairs of hole and electron accordingly. So, the charge generation rate can be rewritten as:

$$G_{(x)} = \int_0^{\lambda_0} G(\lambda, x) d\lambda = \int_0^{\lambda_0} \frac{I(\lambda) \times \alpha(\lambda) \times e^{-\alpha(\lambda)x}}{hc/\lambda} d\lambda = \alpha N_0 e^{-\alpha x} \quad (2.16)$$

where, $I_{(\lambda)}$ is the AM1.5 standard solar spectra, which is calculated by NREL, $N = \int_0^{\lambda_0} \frac{I(\lambda)}{hc/\lambda} d\lambda$. Generally, the bandgap energy of perovskite used for theoretical study is 1.55eV. So, using the linear fitting result of incident photon density and bandgap energy, N_0 becomes:
 $0 \approx -2.2 \times 10^{17} \times 1.55 + 5.12 \times 10^{17} = 1.71 \times 10^{17}$ [17].

In the device, all of the carriers will move to their corresponding electrode, and when they move, electrons and holes will try to recombine. There are two kinds of common recombination mechanism, which are

direct (band to band) and indirect (RSH) recombination. The direct recombination is caused by the electrons' direct transition between the conduction band and valence band. Generally, it is used to describe the device with low defect concentration. It can be expressed as [18]

$$R = \gamma(np - n_{int}^2) \quad (2.17)$$

$$n_{int} = N_c \exp\left(-\frac{E_{gap}}{2V_t}\right) \quad (2.18)$$

$$\gamma = \frac{q\mu}{\epsilon} \quad (2.19)$$

where, γ is the recombination coefficient, and n_{int} is the intrinsic carrier concentration. The indirect recombination is used to describe the device with high defect concentration, and the recombination occurs in the traps and defect centers. It can be given by [18]

$$R = \frac{np - n_{int}^2}{\tau_p(n + n_1) + \tau_n(p + p_1)} \quad (2.20)$$

where, τ_n is the lifetime of the electron, τ_p is the lifetime of the hole. In this model, it ignores the trap and defect concentrations, so only considers the direct recombination mechanism.

Numerical Simulation Method

Poisson's equation and continuity equations are partial differential equations, which are difficult to solve directly by using conventional methods. Therefore, numerical computation approaches are used in the simulation in order to obtain the numerical solutions. In this simulation, the device works under small current and voltage conditions; the coupling between the equations is not significant, so finite difference method and Gummel iteration method are chosen to process these equations.

Discretization of Equations

Finite difference method is a discrete approximation computation approach for differential equations; its calculation results are not a continuous function in the domain but the approximate value of the functions at each mesh point. The basic idea of the difference method is to use different coefficients to replace the derivative part in the equations. In this simulation, it assumes the thickness of perovskite is L nm, and discretises the domain $[0, L]$ with the distance of h . Here, in order to obtain convenient calculation and accurate results, nested grid method is used to discretise the device. The meshing diagram of the device can be shown in Fig.2.01.

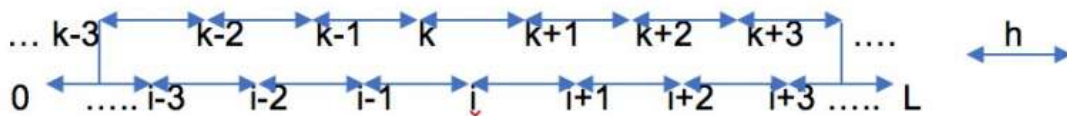


Fig.2.01 Meshing diagram of device

Based on the discretisation model of the device, the Poisson's equation and continuity equations with the discrete form can be described by:

$$\frac{[\varphi(i+1) - \varphi(i)] - [\varphi(i) - \varphi(i-1)]}{h^2} = n(i) - p(i) \quad (2.21)$$

$$\frac{J_n(i) - J_n(i-1)}{h} + qG - qR = 0 \quad (2.22)$$

$$\frac{J_p(i) - J_p(i-1)}{h} - qG + qR = 0 \quad (2.23)$$

where, $k=1,2, 3, \dots, N-1, i=1, 2, \dots, N$, k is the middle point between $i-1$ and I , N is the number of the mesh point. The Scharfetter Gummel approach assumes the change of electric field, carrier mobility and current density can be ignored between i and $i+1$, so that Eq.2.06 and Eq.2.07 become:

$$J_n(i) = \frac{\mu_n q}{h} [\varphi(i) - \varphi(i+1)] \frac{n(i+1)e^{\frac{(\varphi(i)-\varphi(i+1))}{V_t}} - n(i)}{[e^{\frac{(\varphi(i)-\varphi(i+1))}{V_t}} - 1]} \quad (2.24)$$

$$J_p(i) = \frac{\mu_p q}{h} [\varphi(i) - \varphi(i+1)] \frac{p(i)e^{\frac{(\varphi(i)-\varphi(i+1))}{V_t}} - p(i+1)}{[e^{\frac{(\varphi(i)-\varphi(i+1))}{V_t}} - 1]} \quad (2.25)$$

There are after substituting Eq.2.24 and Eq.2.25 into the Poisson's equation and continuity equations.

$$\begin{cases} F_n\{n(i-1), n(i), n(i+1), p(i), \varphi(i-1), \varphi(i), \varphi(i+1))\} = 0 & (2.26) \\ F_p\{p(i-1), p(i), p(i+1), n(i), \varphi(i-1), \varphi(i), \varphi(i+1))\} = 0 & (2.27) \\ F_\varphi\{n(i), p(i), \varphi(i-1), \varphi(i), \varphi(i+1)\} = 0 & (2.28) \end{cases}$$

Here, we have $3 \times (N - 2)$ equations with the boundary conditions, so the numerical solutions can be obtained.

Linearization of Equations

It can be easily seen that J_n, J_p and R are non-linear functions, so that Eq.2.26, Eq.2.27 and Eq.2.28 are non-linear equations too. It is necessary to linearize these equations by using Taylor expansion in order to simplify the computation. According to the theory of the Gummel iteration method, when one variable is calculated we are assuming that other variables are constants. So, when we calculate it needs to keep n and p as constants. Using the first order Taylor expansion at $\varphi_{i-1}^0, \varphi_i^0, \varphi_{i+1}^0$ the Eq.2.28 can be rewritten as

$$F_\varphi = \frac{\partial F_\varphi^0}{\partial \varphi(i-1)} \Delta\varphi(i-1) + \frac{\partial F_\varphi^0}{\partial \varphi(i)} \Delta\varphi(i) + \frac{\partial F_\varphi^0}{\partial \varphi(i+1)} \Delta\varphi(i+1) + F_\varphi^0 = 0 \quad (2.29)$$

In order to ensure the convergence and the accuracy of results, the relationships between φ and n, p need to be considered:

$$\begin{cases} n(i) = n_{int} \exp\left[\frac{\varphi(i) - E_{fn}(i)}{V_t}\right] & (2.30) \\ p(i) = n_{int} \exp\left[\frac{E_{fp}(i) - \varphi(i)}{V_t}\right] & (2.31) \end{cases}$$

Each coefficient in Eq.2.29 is shown below:

$$\begin{cases} \frac{\partial F_\varphi^0}{\partial \varphi(i-1)} = \frac{1}{h^2} \\ \frac{\partial F_\varphi^0}{\partial \varphi(i)} = -\frac{2}{h^2} - \frac{q}{\epsilon} \frac{p^0(i) + n^0(i)}{V_t} \\ \frac{\partial F_\varphi^0}{\partial \varphi(i+1)} = \frac{1}{h^2} \\ F_\varphi^0 = \frac{1}{h^2} \varphi^0(i-1) - \frac{2}{h^2} \varphi^0(i) + \frac{1}{h^2} \varphi^0(i+1) + \frac{q}{\epsilon} [p^0(i) - n^0(i)] \end{cases} \quad (2.32)$$

Here, the chasing method is chosen to solve the equations. This is because the elements of coefficient matrixes are very small, and some of them are approximately zero, where it is possible to make the coefficient

matrixes become a tri-diagonal matrix. In addition, these matrixes meet the limitation conditions of the chasing method.

Solve the Poisson's equation in an independent loop until ϕ meets the accuracy condition. After getting new potential values, we substitute them into the continuity equations to calculate n and p respectively. When n is calculated, maintain ϕ and p as constants. Using the first order Taylor expansion at $n_{i-1}^0, n_i^0, n_{i+1}^0$ the Eq.2.26 becomes:

$$F_n = \frac{\partial F_n^0}{\partial n(i-1)} \Delta n(i-1) + \frac{\partial F_n^0}{\partial n(i)} \Delta n(i) + \frac{\partial F_n^0}{\partial n(i+1)} \Delta n(i+1) + F_n^0 = 0 \quad (2.33)$$

$$\begin{cases} \frac{\partial F_n^0}{\partial n(i-1)} = \frac{\mu_n}{h^2} \frac{[\varphi(i-1) - \varphi(i)]}{\exp\left[\frac{\varphi(i-1) - \varphi(i)}{V_t}\right] - 1} \\ \frac{\partial F_n^0}{\partial n(i)} = -\frac{\mu_n}{h^2} [\varphi(i-1) - \varphi(i)] \frac{\exp\left[\frac{\varphi(i-1) - \varphi(i)}{V_t}\right]}{\exp\left[\frac{\varphi(i-1) - \varphi(i)}{V_t}\right] - 1} - \frac{\mu_n}{h^2} \frac{[\varphi(i) - \varphi(i+1)]}{\exp\left[\frac{\varphi(i) - \varphi(i+1)}{V_t}\right] - 1} - \gamma p^0(i) \\ \frac{\partial F_n^0}{\partial n(i+1)} = \frac{\mu_n}{h^2} [\varphi(i) - \varphi(i+1)] \frac{\exp\left[\frac{\varphi(i) - \varphi(i+1)}{V_t}\right]}{\exp\left[\frac{\varphi(i) - \varphi(i+1)}{V_t}\right] - 1} \\ F_n^0 = \frac{\partial F_n^0}{\partial n(i-1)} n^0(i-1) + \left[\frac{\partial F_n^0}{\partial n(i)} + \gamma p^0(i)\right] n^0(i) + \frac{\partial F_n^0}{\partial n(i+1)} n^0(i+1) + G(i) - R(i) \end{cases} \quad (2.34)$$

The first order Taylor expansion form of Eq.2.28 can be obtained by using the same approach, as shown previously. The results are shown in Eq.2.35 and Eq. 2.36.

$$F_p = \frac{\partial F_p^0}{\partial p(i-1)} \Delta p(i-1) + \frac{\partial F_p^0}{\partial p(i)} \Delta p(i) + \frac{\partial F_p^0}{\partial p(i+1)} \Delta p(i+1) + F_p^0 = 0 \quad (2.35)$$

$$\begin{cases} \frac{\partial F_p^0}{\partial p(i-1)} = -\frac{\mu_p}{h^2} [\varphi(i-1) - \varphi(i)] \frac{\exp\left[\frac{\varphi(i-1) - \varphi(i)}{V_t}\right]}{\exp\left[\frac{\varphi(i-1) - \varphi(i)}{V_t}\right] - 1} \\ \frac{\partial F_p^0}{\partial p(i)} = \frac{\mu_p}{h^2} [\varphi(i) - \varphi(i+1)] \frac{\exp\left[\frac{\varphi(i) - \varphi(i+1)}{V_t}\right]}{\exp\left[\frac{\varphi(i) - \varphi(i+1)}{V_t}\right] - 1} - \frac{\mu_p}{h^2} \frac{[\varphi(i-1) - \varphi(i)]}{\exp\left[\frac{\varphi(i-1) - \varphi(i)}{V_t}\right] - 1} + \gamma n^0(i) \\ \frac{\partial F_p^0}{\partial p(i+1)} = -\frac{\mu_p}{h^2} \frac{[\varphi(i) - \varphi(i+1)]}{\exp\left[\frac{\varphi(i) - \varphi(i+1)}{V_t}\right] - 1} \\ F_p^0 = \frac{\partial F_p^0}{\partial p(i-1)} p^0(i-1) + \left[\frac{\partial F_p^0}{\partial p(i)} - \gamma n^0(i)\right] p^0(i) + \frac{\partial F_p^0}{\partial p(i+1)} p^0(i+1) - G(i) + R(i) \end{cases} \quad (2.36)$$

After solving the continuity equations for electrons and holes, it is needed to be estimated whether n and p meet the accuracy condition. If these solutions meet the accuracy condition, the iteration loop is stopped and J_n and J_p are calculated. On the contrary, the new carrier densities (n and p) are substituted into the Poisson's equation and a new iteration is started until all the solutions meet the accuracy condition. The Gummel iteration method flow diagram is shown in Fig.2.02.

II. RESULTS AND DISCUSSION

The parameters used in the simulation are summarised in Table.2.1. The parameters are extracted from literature [19].

Table.2.1 Parameters used in the simulation

| Parameters | Symbol | Value |
|------------------------|----------|-----------------------------------|
| Absorption coefficient | α | $5.7 \times 10^4 \text{ cm}^{-1}$ |
| Hole mobility | μ_p | $2 \text{ cm}^2/\text{Vs}$ |
| Temperature | T | 300 K |
| Electron mobility | μ_n | $1 \text{ cm}^2/\text{Vs}$ |

| | | |
|----------------------------------|------------|--------------------------------------|
| Band gap | E_{gap} | 1.55 eV |
| Perovskite thickness | L | 100nm |
| Relative dielectric permittivity | ϵ | 30 |
| Density of state | N_c | $2.2 \times 10^{18} \text{ cm}^{-3}$ |

Table.2.2 The values of Isc, Voc, and FF for different Nc

| N_c/cm^{-3} | Isc/mA/cm-2 | Voc/V | FF |
|----------------------|-------------|-------|-------|
| 10^{18} | 11.4 | 1.072 | 0.778 |
| 10^{19} | 11.2 | 0.939 | 0.761 |
| 10^{20} | 10.9 | 0.833 | 0.738 |
| 10^{21} | 10.7 | 0.701 | 0.747 |

It can be seen that N_c has a significant influence on the device performance in particular on Voc, when it is changed. With the increase of N_c , the short-circuit current density slowly decreases, the open-circuit voltage increases rapidly, and the fill factor changes irregularly.

Fig.2.04 and Fig.2.05 show the carriers distribution in the device for $N_c=10^{18} \text{ cm}^{-3}$ and $N_c=10^{20} \text{ cm}^{-3}$ respectively. It can be seen that the densities of minority carriers almost remain the same when N_c is changed from $N_c=10^{18} \text{ cm}^{-3}$ to $N_c=10^{20} \text{ cm}^{-3}$ but the majority carriers increase significantly. This can be explained by the Poisson's equation with the electric field form

$$\frac{\partial E_{field}}{\partial x} = \frac{q}{\epsilon}(n - p).$$

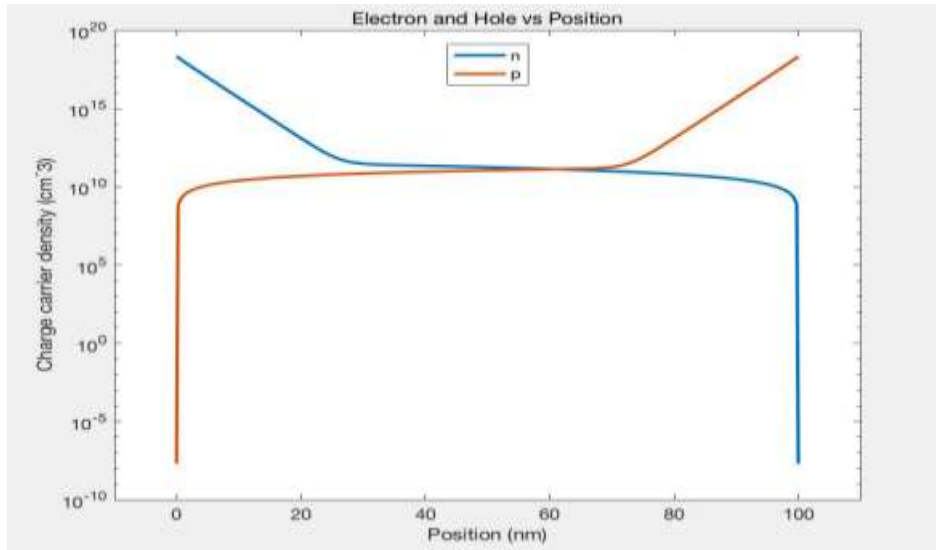


Fig.2.04 Charge carriers' distribution for $N_c=10^{18} \text{ cm}^{-3}$

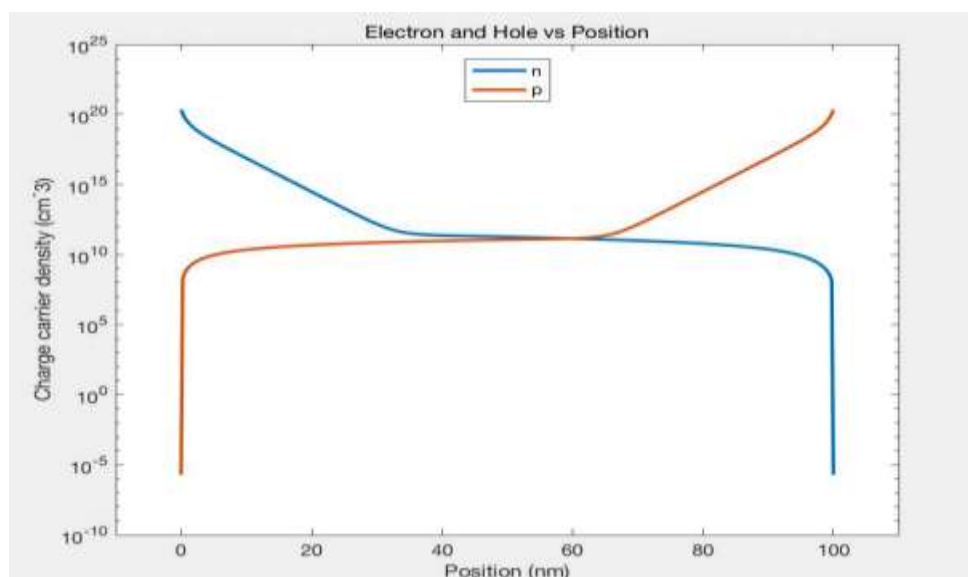


Fig.2.05 Charge carriers' distribution for $N_c=10^{20} \text{ cm}^{-3}$

Fig.2.06 illustrates the potential distribution for $N_c=10^{18} \text{ cm}^{-3}$ and $N_c=10^{20} \text{ cm}^{-3}$ respectively. When N_c is small, the potential distribution is nearly linear. When N_c is large, the potential changes rapidly at both sides of the device but it changes minimal in the middle of the device.

III. CONCLUSION

A numerical model for perovskite solar cell and a specific computation process for Poisson's equation and continuity equations mainly introduces by this chapter. The simulation results are obtained by using the Matlab program. The influence of effective density of state, relative dielectric permittivity, and band gap energy on device performance is investigated. Through the analysis of the simulation results, it is found that a large value of effective density state can decrease open-circuit voltage significantly, meanwhile it can also decrease the short-circuit current slightly. Thus, in order to obtain good device performance, it is necessary to choose a small value of effective density state material or control the density of state of the material used in the absorber layer.

REFERENCE

- [1]. B.A. Rosales et al., Synthesis and mixing of complex halide perovskites by solvent-free solid-state methods *J. Solid State Chem.* (2019).
- [2]. Y. Chen et al., SnO_2 -based electron transporting layer materials for perovskite solar cells: A review of recent progress; *Journal of Energy Chemistry*; (2019)
- [3]. P. Hankare et al. WS_2 thin films: Opto-electronic characterization; *J. Alloy. Compd.* (2009).
- [4]. M. Saliba et al. How to make over 20% efficient perovskite solar cells in regular (n-i-p) and inverted (p-i-n) architectures; *Chem. Mater.* (2018).
- [5]. A. Kojima et al. Organometal halide perovskites as visible-light sensitizers for photovoltaic cells; *J. Am. Chem. Soc.* (2009)
- [6]. H.S. Kim et al. Lead iodide perovskite sensitized all-solid-state submicron thin film mesoscopic solar cell with efficiency exceeding 9%; *Sci. Rep.* (2012)
- [7]. M. Liu et al. Efficient planar heterojunction perovskite solar cells by vapour deposition; *Nature* (2013)
- [8]. H. Zhou et al. Interface engineering of highly efficient perovskite solar cells; *Science*, (2014)
- [9]. W.S. Yang et al. High-performance photovoltaic perovskite layers fabricated through intramolecular exchange; *Science*; (2015).
- [10]. Basore, P. A. (1990). Numerical modeling of textured silicon solar cells using PC- 1D. *IEEE Transactions on electron devices*, 37(2), 337-343.
- [11]. Jerry G. Fossum. Computer-aided numerical analysis of silicon solar cells. *Solid. State. Electron.*, 19(4):269-277, Apr 1976.
- [12]. Lee, C., Efsthadiadis, H., Raynolds, J. E., & Haldar, P. (2009, June). Two-dimensional computer modeling of single junction a-Si: H solar cells. In *Photovoltaic Specialists Conference (PVSC), 2009 34th IEEE* (pp. 001118-001122). IEEE.

- [13]. Kei Ogiya, Chen Lv, Ai Suzuki, et al. Development of Multiscale Simulator for Dye-Sensitized TiO₂Nanoporous Electrode Based on Quantum Chemical Calculation. *Jpn. J. Appl. Phys.*, 47(4):3010–3014, 2008.
- [14]. Julio Villanueva, Juan A Anta, Elena Guillen, and Gerko Oskam. Numerical Simulation of the CurrentVoltage Curve in Dye-Sensitized Solar Cells. *J. Phys. Chem. C*, 113(45):3–4, November 2009.
- [15]. Jinhua Cai and Liyuan Han. Theoretical Investigation on Interfacial-Potential- Limited Diffusion and Recombination in Dye-Sensitized Solar Cells. *J. Phys. Chem. C*, 115(34):17154–17162, September 2011.
- [16]. Hoppe, H., Arnold, N., Meissner, D., & Sariciftci, N. S. (2004). Modeling of optical absorption in conjugated polymer/fullerene bulk-heterojunction plastic solar cells. *Thin Solid Films*, 451, 589-592.
- [17]. Zhou, Y., Huang, F., Cheng, Y. B., & Gray-Weale, A. (2017). Numerical analysis of a hysteresis model in perovskite solar cells. *Computational Materials Science*, 126, 22-28.
- [18]. Fonash, S. (2012). *Solar cell device physics*. Elsevier.
- [19]. Tan, K., Lin, P., Wang, G., Liu, Y., Xu, Z., & Lin, Y. (2016). Controllable design of solid-state perovskite solar cells by SCAPS device simulation. *Solid-State Electronics*, 126, 75-80.